PHYSICAL REVIEW APPLIED **13,** 024021 (2020)

Protecting Quantum Spin Coherence of Nanodiamonds in Living Cells

Q.-Y. Cao,[1,2] P.-C. Yang,[1,2,†] M.-S. Gong,[1,2] M. Yu,[1,2] A. Retzker,[3] M.B. Plenio,[4,2] C. Müller,[5]
N. Tomek,[5] B. Naydenov,[5] L.P. McGuinness,[5] F. Jelezko,[5,2] and J.-M. Cai[1,2,*]

[1] *School of Physics and Wuhan National Laboratory for Optoelectronics, Huazhong University of Science and Technology, Wuhan, 430074, China*
[2] *International Joint Laboratory on Quantum Sensing and Quantum Metrology, Huazhong University of Science and Technology, Wuhan, 430074, China*
[3] *Racah Institute of Physics, The Hebrew University of Jerusalem, 91904 Jerusalem, Israel*
[4] *Institut für Theoretische Physik and IQST, Universität Ulm, Albert-Einstein-Allee 11, 89081 Ulm, Germany*
[5] *Institut für Quantenoptik and IQST, Universität Ulm, Albert-Einstein-Allee 11, 89081 Ulm, Germany*

(Received 11 December 2017; revised manuscript received 8 January 2020; accepted 10 January 2020;
published 10 February 2020)

Because of its superior coherent and optical properties at room temperature, the nitrogen-vacancy (N-V) center in diamond has become a promising quantum probe for nanoscale quantum sensing. However, the application of N-V-containing nanodiamonds to quantum sensing suffers from their relatively short spin coherence times. Here we demonstrate energy-efficient protection of N-V spin coherence in nanodiamonds using concatenated continuous dynamical decoupling, which exhibits excellent performance with a less-stringent microwave-power requirement. When this is applied to nanodiamonds in living cells, we are able to extend the spin coherence time by an order of magnitude to the T_1 limit of 30 μs. Further analysis demonstrates concomitant improvements of sensing performance, which shows that our results provide an important step toward *in vivo* quantum sensing using N-V centers in nanodiamond.

DOI: 10.1103/PhysRevApplied.13.024021

I. INTRODUCTION

Nitrogen-vacancy (N-V) centers in diamond exhibit stable fluorescence and have a spin triplet ground state, which can be coherently manipulated by microwave fields [1]. Observation of spin-dependent fluorescence provides an efficient way to read out the spin state of N-V centers. The energy splitting of the N-V spin depends on physical parameters, such as a magnetic field [2–4], an electric field [5,6], temperature [7–10], and pressure [11,12]. A variety of quantum-sensing protocols for precise measurement of these physical parameters in different scenarios have been developed [13–26]. These protocols are all based on determining the N-V spin energy splitting, which is why the measurement sensitivity is limited by the N-V spin coherence time.

Spin coherence in bulk diamond is affected mainly by surrounding electronic impurities (P1 centers) and nuclear spins (natural abundance of ^{13}C isotope). The spin reservoir can be eliminated by use of isotopically engineered high-purity type-IIa diamond [27]. To mitigate the influence of any residual impurities, pulsed dynamical decoupling has been widely used to prolong the spin coherence time [28–30]. Its excellent performance when applied to N-V centers in bulk diamond is a result of the quasistatic characteristics of the spin reservoir in bulk diamond and the high available microwave power. Unfortunately, these two factors may not be satisfied for N-V centers in nanodiamonds, which are required for sensing applications *in vivo*. N-V centers contained within nanodiamonds typically exhibit a long spin coherence time, which has been attributed to nanodiamond surface spin noise and electric charge noise that include prominent high-frequency components. Preserving the coherence of N-V centers in nanodiamonds becomes even more problematic when they are located in biological environments, which present additional noise sources. The microwave power available to decouple N-V centers in living cells can be limited by the large distance between the microwave antenna and the nanodiamond, and the damaging effects that microwave absorption may have on biological tissue. Therefore, the development of an energy-efficient strategy to prolong the coherence time of N-V centers in nanodiamond under the constraint of limited microwave power is a significant challenge for efficient quantum-sensing protocols for biology and nanomedicine [8,31–35].

In this work, we address this key challenge with the implementation of concatenated continuous dynamical decoupling (CCDD), which uses a microwave driving field

---

[*] jianmingcai@hust.edu.cn
[†] pengchengyang@hust.edu.cn

consisting of suitably engineered multifrequency components [36–38] to prolong the coherence time of N-V centers contained within nanodiamonds. The purpose of the main frequency component of the microwave drive is to suppress fast environmental noise, while the other, weaker frequency components compensate power fluctuations in the main frequency component. The key advantage of CCDD compared with pulsed schemes is that the decoupling efficiency achievable at the same average power (as quantified by the effective Rabi frequency $\bar{\Omega}^2 = \langle \Omega^2 \rangle$ averaged over time) is predicted theoretically to be superior to that of pulsed schemes [35]. We demonstrate experimentally that CCDD achieves a performance that significantly exceeds that of pulsed-dynamical-decoupling strategies given the same microwave-energy consumption. We show that CCDD prolongs the coherence time of N-V centers in nanodiamond up to tens of microseconds, at which point it reaches the limit imposed by the N-V spin relaxation time T_1 in these nanodiamonds inside living cells. Our result is an important step toward the development of quantum sensing for *in vivo* applications with high achievable sensitivity, and also demonstrates wide applications of quantum control using an amplitude- and phase-modulated driving field [39,40].

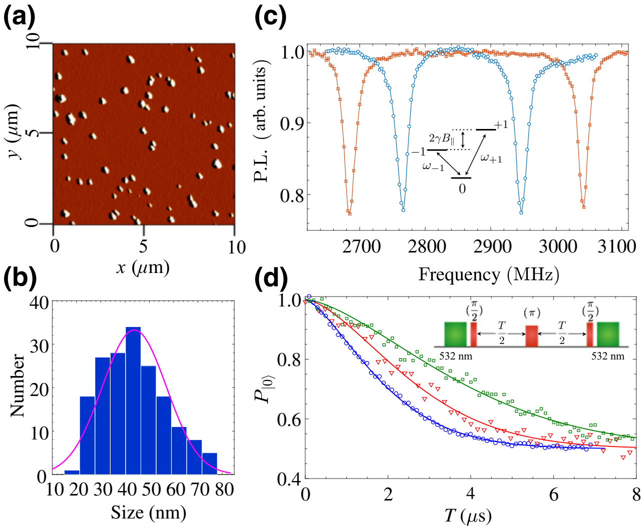

FIG. 1. Characteristics of N-V centers in nanodiamond. (a) Atomic-force-microscope image of nanodiamonds deposited on a mica plate. (b) Histogram of nanodiamond sizes that predominantly range from 25 to 61 nm (43 ± 18 nm). (c) Typical ODMR measurement of a nanodiamond N-V center with applied magnetic field $B_{\|} = 37.8$ G (□) and $B_{\|} = 66$ G (○). (d) Time evolution of the spin-state population $P_{|0\rangle}$ in the spin-echo experiment for three typical N-V centers. By fitting the data with a function of the form $(1/2)\{1 + \exp[-(T/T_{\mathrm{SE}})^{\alpha}]\}$, we estimate the parameters T_{SE} and α as follows: 2.142 ± 0.018 μs and 1.448 ± 0.026 (N-V 1, ○); 4.292 ± 0.133 μs and 1.47 ± 0.10 (N-V 2, □); 2.990 ± 0.083 μs and 1.576 ± 0.101 (N-V 3, ▽). P.L., Photoluminescence.

II. PROTECTING COHERENCE OF N-V SPIN IN NANODIAMOND

In our experiment, we use nanodiamonds obtained by milling of high-pressure, high-temperature diamond from Microdiamant with diameters of approximately 43 ± 18 nm, as measured with an atomic force microscope (AFM); see Figs. 1(a) and 1(b). We apply a static external magnetic field of strength B along the N-V axis, which leads to two allowed N-V spin transitions ($m_s = 0 \leftrightarrow m_s = +1$ and $m_s = 0 \leftrightarrow m_s = -1$). The corresponding optically-detected-magnetic-resonance (ODMR) measurement is shown in Fig. 1(c). We first characterize the coherence properties of single N-V centers in nanodiamonds by performing spin-echo measurements. Microwave control pulses are generated with an arbitrary-waveform generator (AWG) and are amplified by a microwave amplifier. The power of the microwave radiation determines the frequency of Rabi oscillation. Spin-echo measurements are performed for several N-V centers to determine the spin coherence time; three representative examples are shown in Fig. 1(d). The data are fitted by a decay function in the form of $\exp[-(t/T_{\mathrm{SE}})^{\alpha}]$, where T_{SE} denotes the spin-echo coherence time. We extract the value of α, and find that $\alpha \in [1.08, 1.74]$, indicating decoherence is due to both slow and fast environmental fluctuations; see Appendixes A–F. Universal dynamical decoupling with a train of pulses, such as Carr-Purcell-Meiboom-Gill and XY8 sequences, may prolong the spin coherence time by suppressing noise of low frequency [29,30]. Our Ramsey measurement under different magnetic field strengths shows that T_2^* becomes greater as the magnetic field increases (see Appendixes A–F), which suggests that the noise in the present scenario is dominated by surface electric noise [41] rather than a slow-spin bath.

We apply XY8-N pulse sequences to several N-V centers using a train of $8N$ π pulses, as shown in Fig. 2(a). Figure 2(b) shows the measurement results obtained by our applying up to 96 π pulses. The extended coherence time T_2 under dynamical decoupling increases as the number of XY8 cycles grows following the scaling $(N^{-\beta} + T_{\mathrm{SE}}/T_1)^{-1}$, with N up to 12 [42]; see Fig. 2(c). We also observe that the coherence time saturates and any further increase of the number of pulses does not necessarily lead to a longer coherence time. Because the XY8 pulse sequence exhibits excellent pulse-error tolerance [43], the experimental observation suggests that the limited coherence time is likely due to fast noise dynamics and limited microwave power (pulse repetition rate).

To achieve high-efficiency dynamical decoupling under the constraint of microwave power, we apply CCDD to protect spin coherence of nanodiamond N-V centers. We begin by illustrating the basic idea of CCDD as applied to the $m_s = 0 \leftrightarrow m_s = -1$ transition of a single N-V spin

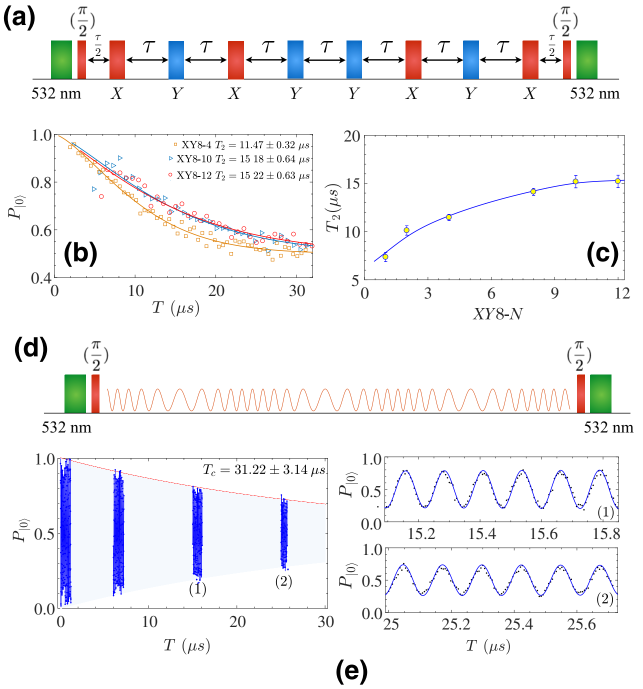

FIG. 2. Performance of concatenated continuous dynamical decoupling as compared with XY8 pulsed dynamical decoupling. (a) XY8 pulse sequence. (b) Coherence time of nanodiamond N-V is extended by an XY8-N pulse sequence with the number of pulses up to 96 ($8 \times N$). The Rabi frequency of the π pulse is 8.5 MHz. The data are fitted with the decay function $(1/2)\{1 + \exp[-(T/T_2)^\alpha]\}$, which indicates an achievable coherence time $T_2 = 15.22 \pm 0.63$ μs. (c) Scaling of T_2 with the number of XY8 cycles N, which fits $(N^{-\beta} + T_{\mathrm{SE}}/T_1)^{-1}$ [42] with $\beta = 0.319 \pm 0.064$. (d) Concatenated continuous dynamical decoupling scheme with phase-modulated driving. (e) The extended spin coherence time by CCDD reaches $T_c = 31.22 \pm 3.14$ μs. The signal envelope is fitted by $(1/2)\{1 + \exp[-(T/T_c)]\}$. The driving parameters are $\Omega_1 = 8.06$ MHz and $\Omega_2/\Omega_1 = 0.1$. Subpanels 1 and 2 show enlarged over different measurement intervals. The applied magnetic field $B_\parallel = 508$ G.

[36–38]. The present scheme is applicable to many other two-level quantum systems. We introduce a microwave driving field with phase modulation [37] as

$$\tilde{H} = (\Omega_1 + \delta_x)\cos\left[\omega_0 t + 2\left(\frac{\Omega_2}{\Omega_1}\right)\sin\Omega_1 t\right]\sigma_x, \qquad (1)$$

where σ_x is the Pauli operator, ω_0 is the energy gap between $m_s = 0$ and $m_s = -1$, Ω_1 is the Rabi frequency as determined by the microwave power, Ω_2 denotes the ratio of phase modulation, and the fluctuation in microwave power is denoted as δ_x. The effect of magnetic noise is suppressed by the driving field as long as the noise power density is small at frequency Ω_1. In the interaction picture, the effective Hamiltonian can be written as [37] $H_{I2} = -\Omega_2/2\sigma_z + \delta_x\sigma_x$. As the phase control in the AWG is very stable, the fluctuation in Ω_2 is negligible. As long as the power spectrum of δ_x is negligible at frequencies larger than Ω_2, the noise will lead to only a second-order effect; that is, $\delta_x^2/\Omega_2\sigma_z$ [44]. As compared with pulsed-dynamical-decoupling strategy, CCDD can achieve better performance with the same average microwave power [35] as we confirm in our experiment on nanodiamonds in living cells. A schematic of the microwave and readout sequence to implement CCDD in our experiment is shown in Fig. 2(d). A $\pi/2$ pulse prepares the N-V spin in a superposition state of $|0\rangle$ and $|-1\rangle$. The phase-varying driving field as in Eq. (1) is generated with an AWG and acts on the N-V spin for time T. A final $\pi/2$ pulse maps spin coherence information into the state $|0\rangle$ population as measured by an avalanche-photodiode gate. Figure 2(e) shows coherent oscillation resulting from our applying the CCDD scheme, which leads to an extended coherence time $T_c = 31.22 \pm 3.14$ μs, which is of the same order as the relaxation time T_1 (which we measure to be 87.35 ± 7.50 μs) as T_2 is limited by $T_1/2$ [45].

The requirement of low microwave power is of practical importance for quantum-sensing applications *in vivo*, because microwave radiation is absorbed by biological tissues, which may lead to heating and subsequent damage or denaturing of protein molecules. To demonstrate the performance of CCDD aimed at biosensing, we use the scheme to protect the spin coherence of N-V centers in nanodiamonds taken up by living cells. We use NIH/3T3 cells, which are adherent to the upper surface of the cover glass. To avoid the strong fluorescence of the nutrient solution, we replace it with phosphate-buffered saline (PBS), which has almost no fluorescence, and wash the cells 3 times to remove nanodiamonds not internalized by the cells. Figure 3(a) shows a confocal-scan image of the cell sample where fluorescence is gated around the N-V emission spectrum. With membrane labeling and depth-scan tomography, we clearly identify nanodiamonds that are taken up by the cells and located in the cell cytosol. We perform ODMR measurements [Fig. 3(b)] and spin-echo measurements [Fig. 3(c)] to characterize the properties of those nanodiamond N-V centers in cells. We compare the performance of CCDD with XY8 pulsed dynamical decoupling for the protection of N-V spin coherence in cells. Figures 3(c) and 3(d) show the measurement data obtained by our applying microwaves of power that corresponds to a Rabi frequency of 9.6 MHz in XY8 pulsed dynamical decoupling and 4.6 MHz in the CCDD scheme. The N-V spin coherence time is increased up to 29.4 ± 3.6 μs by the CCDD scheme, while XY8 pulsed scheme achieves only 17.49 ± 1.43 μs. The advantage of CCDD scheme becomes more prominent as the available microwave power is reduced and T_1 is increased by nanodiamond-material design. To characterize the damage caused by microwave radiation, we apply the experimental sequences and monitor the temperature increase of the sample. The results suggest that the temperature increase due to the pulse sequences is about 10 °C

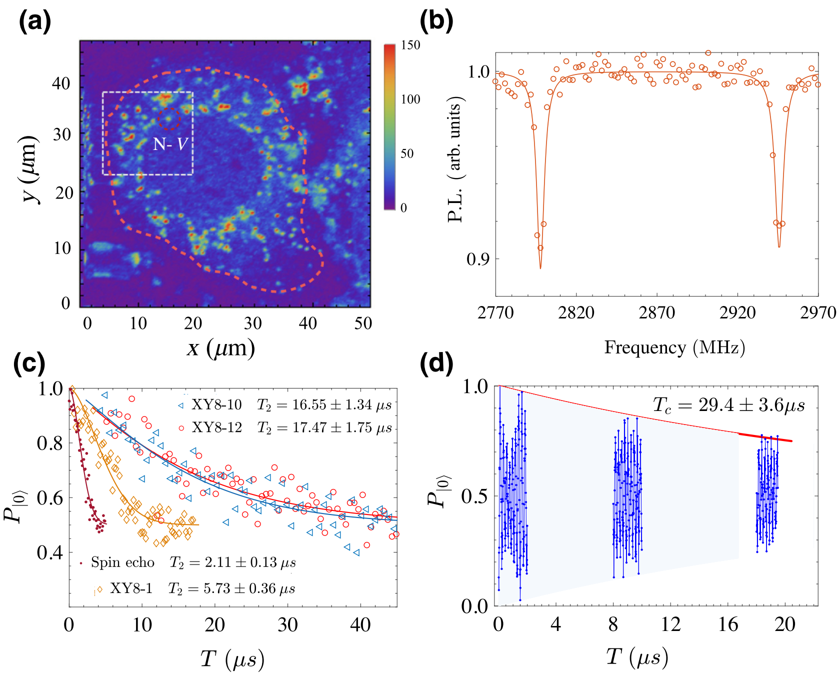

FIG. 3. Protecting quantum spin coherence in living cells. (a) Confocal image of a cell with uptake of fluorescent nanodiamonds. The red curve indicates the cell boundary. The nanodiamonds in the dashed rectangle are located in the cytoplasm. The photon counts are in the unit of 1000 counts/s. (b) ODMR measurement of a nanodiamond N-V center in a cell with applied magnetic field $B_{\parallel} = 25$ G. (c) N-V coherence time in a living cell is extended by spin-echo and XY8 pulse sequences (XY8-N) with the number of pulses up to 96. The Rabi frequency of the π pulse is 9.6 MHz. (d) The CCDD signal indicates a spin coherence time of 29.4 ± 3.6 μs with Rabi frequency $\Omega_1 = 4.6$ MHz and $\Omega_2 = \Omega_1/10$. P.L., Photoluminescence.

more than that due to CCDD for the achievement of similar coherence times; see Appendixes A–F. Such a difference in the temperature increase is expected to have a significant effect on biological tissue [46,47].

Apart from avoiding the damaging effect on biological tissues (which is dependent mainly on the average microwave power), the constraint of microwave power on pulsed-dynamical-decoupling efficiency when combined with (*in vivo*) quantum sensing may arise from another origin. The maximal microwave power, which determines the achievable Rabi frequency, may be limited by, for example, the relatively large distance between the microwave antenna and the nanodiamond especially when compared with bulk-diamond experiments. We perform CCDD measurements using different peak microwave powers and compare the results with the longest possible coherence times that are achieved by XY8 pulsed dynamical decoupling. Our results as shown in Fig. 4(a) demonstrate that given the same effective Rabi frequency (i.e., the same average microwave power), the CCDD scheme clearly outperforms the XY8 dynamical decoupling sequences in extending the spin coherence time. Unlike the XY8 pulsed scheme, where the decoupling efficiency in our experiments is limited by the constraint of microwave power, the coherence time achieved by CCDD is predominantly limited by the T_1 time of nanodiamonds, which can be increased by material design.

III. APPLICATION IN QUANTUM SENSING

For sensing applications inside living cells, one has to take the constraint of microwave power arising from both origins discussed above into account. We consider a typical scenario of detecting an oscillating magnetic field with frequency ω_s. The underlying principle is essentially similar to the detection of electron (nuclear) spin, where the characteristic frequency is the Larmor frequency of the target spins. One potential interesting example is the detection of the emergence or disappearance of radicals and functional-molecule groups of nuclear spins. The pulsed scheme detects the field by engineering the time interval τ_p between pulses to match the field frequency; namely, $\tau_c = k(\pi/\omega_s)$. For ideal instantaneous π pulses (requiring infinite microwave power), the estimated

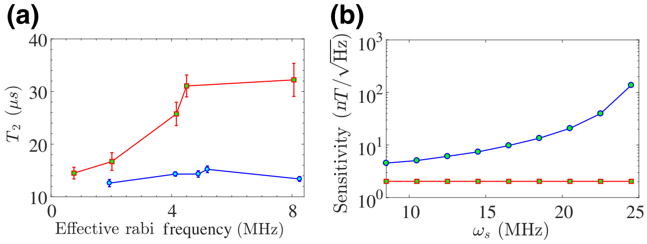

FIG. 4. (a) Extended coherence times as achieved by the CCDD scheme (□) and XY8 pulsed dynamical decoupling (○) as a function of the effective Rabi frequency. The number of XY8 cycles (up to 12) that achieve the longest possible coherence time is given in Table II. (b) Estimated sensitivity for the measurement of an oscillating field using the CCDD scheme (□) and the XY8 scheme (○). The achievable Rabi frequency is $\Omega = 8.5$ MHz, and the coherence time is assumed to be $T_2 = 15.22$ μs for the XY8 scheme and 31.22 μs for the CCDD scheme. The oscillating field strength $\gamma b = 2\pi \times 100$ kHz. The other experimental parameters are the same as for Fig. 2.

measurement sensitivity $\eta_c = k\pi/4\gamma\sqrt{T_2}$, where γ is the electronic gyromagnetic ratio and for simplicity we assume a unit detection efficiency. However, the limited achievable pulse peak Rabi frequency Ω (in comparison with the field frequency ω_s) leads to a constraint on the resonant condition $k \geq \omega_s/\Omega$ and will decrease the signal contrast. This restricts pulsed schemes to work only for frequencies below approximately 10 MHz when the pulse repetition rate and microwave power are limited, which is quite likely in biological systems. The present CCDD scheme can detect the field on resonance when $\Omega_1 = \omega_s$ and $\omega_0 - \omega_s = \pm\Omega_1$ with estimated measurement sensitivity $\eta_c = 1/\gamma\sqrt{T_c}$ and $2/\gamma\sqrt{T_c}$, respectively [37]. The resonance condition can be satisfied by tuning ω_0 (via the external magnetic field); thus, if one can flexibly choose Ω_1 and Ω_2 following the principle to optimize the increase of the coherence time. Therefore, the advantage of the CCDD scheme as compared with the pulsed scheme in quantum sensing is not only the increase of the coherence time but also its capability to increase sensitivity in the presence of the constraint of limited average microwave power. In Fig. 4(b), we compare the estimated measurement sensitivity for the CCDD scheme and the pulsed scheme under the same average-power constraint. It can be seen that CCDD shows superior performance for signal frequencies above 10 MHz. Potentially interesting examples include the detection of molecules (containing nuclear spins) in high-field magnetic resonance spectroscopy and electron (radicals). Besides the sensitivity enhancement, the CCDD scheme may avoid the misidentification of frequency components in classical fields or single-molecule spectroscopy [48–50] due to the relatively long pulse duration (as the microwave power is not sufficiently high). The present scheme (with both the sensitivity and the linewidth limited by the increased T_2) would thus advance the application of N-*V*-based quantum sensing *in vivo* using nanodiamonds, offering a method complementary to continuous-wave ESR measurement (the sensitivity of which is limited by the small T_2^*) and relaxation spectroscopy (the linewidth of which is limited by T_2^*) [18].

IV. CONCLUSION AND DISCUSSION

To conclude, we implement a concatenated-continuous-dynamical-decoupling strategy to prolong the quantum spin coherence time of N-*V* centers in nanodiamonds even inside living cells. We demonstrate significantly increased performance with a less-stringent requirement with regard to microwave power in comparison with pulsed schemes, thus causing less-severe damage to living cells. The concatenated-continuous-dynamical-decoupling strategy thus provides a valuable tool for achieving long-spin-coherence-time quantum sensors when the available and feasible microwave power is low or has to be limited (e.g., to avoid damage to biological tissue). It also enables relatively-high-frequency magnetic field sensing with a substantial enhancement in the measurement sensitivity. The ability to extend spin coherence times in living cells along with enhanced measurement sensitivity raises new possibilities for the application of nanodiamond-based quantum sensing in the intracellular environment and related biological events.

ACKNOWLEDGMENTS

We thank Jianwei Wang, Quan Gan, Yuzhou Wu, and Yuan Zhuang for help in sample preparation, Michael Ferner, Manfred Bürzele, Z.-J. Shu, J.-Y. He, R.-F. Hu, and H.-B. Liu for technical assistance, and Itsik Cohen for fruitful discussion. We acknowledge support by the National Natural Science Foundation of China (Grants No. 11874024 and No. 11690032) and the Open Project Program of Wuhan National Laboratory for Optoelectronics (Grant No. 2019WNLOKF002). A.R. acknowledges the support of the European Research Council (ERC) (QRES). M.B.P. is supported by the DFG (FOR 1493), the European Union via DIADEMS and HYPERDIAMOND, an ERC Synergy grant (BIOQ), and the Center for Integrated Quantum Science and Technology (IQST). C.M., N.T., B.N., L.P.M., and F.J. are supported by the DFG (FOR 1493, SFB TR21, SPP 1923), VolkswagenStiftung, BMBF, ERC, European Union (DIADEMS), Baden-Württemberg Stiftung, German Ministry of Science and Arts, and IQST.

APPENDIX A: PRINCIPLE OF CONCATENATED CONTINUOUS DYNAMICAL DECOUPLING

To suppress the effect from both environmental noise and microwave fluctuation, we implement concatenated continuous dynamical decoupling by introducing a microwave driving field with time-dependent phase modulation [37]. We repeat here the derivation for self-consistency. We start with the Hamiltonian:

$$H = \frac{\omega_0}{2}\sigma_z + (\Omega_1 + \delta_x)\cos\left[\omega_0 t + 2\left(\frac{\Omega_2}{\Omega_1}\right)\sin\Omega_1 t\right]\sigma_x. \tag{A1}$$

By moving to the interaction picture with respect to

$$H = \left(\frac{\omega_0}{2} + \Omega_2\cos\Omega_1 t\right)\sigma_z, \tag{A2}$$

we get

$$H_1 = \left(\frac{\Omega_1 + \delta_x}{2}\right)\sigma_x - \Omega_2\cos(\Omega_1 t)\sigma_z. \tag{A3}$$

Moving again to the interaction picture with respect to $\Omega_1\sigma_x$, we get

$$H_2 = \delta_x\sigma_x - (\Omega_2/2)\,\sigma_z. \tag{A4}$$

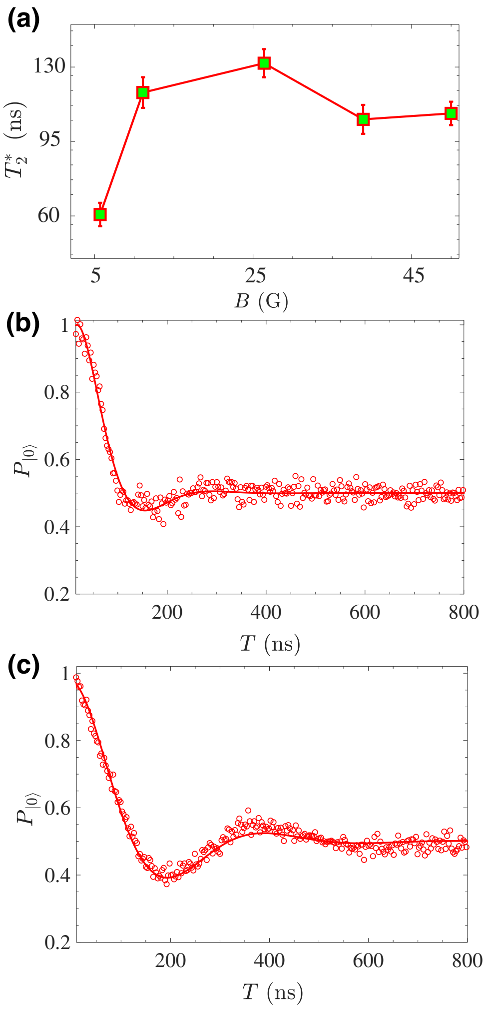

FIG. 5. (a) Dependence of T_2^* on the strength of the magnetic field. (b),(c) Ramsey-measurement data obtained with magnetic field $B = 5$ G (b) and $B = 25$ G (c).

As Ω_2 is generated by the time-dependent phase, we assume that the noise is negligible. As $\Omega_2 \gg \delta_x$ and we assume that the amount of Ω_2 in the power spectrum of δ_x is negligible, the deleterious effect of the noise will manifest itself only in second order; that is,

$$H_{\text{noise}} = \left(\delta_x^2/\Omega_2\right)\sigma_z. \tag{A5}$$

As Ω_2/Ω_1 is kept at 0.1 and δ_x is on the order of 1% of Ω_1, the effect of the noise is on the order of $10^{-3}\Omega_1$. It is noteworthy that this effect could be further suppressed by adding a higher drive by an extra time-dependent-phase term. In our experiment, we first apply a $(\pi/2)_y$ pulse to prepare the N-V-center spin in a superposition state $|\psi(0)\rangle = (1/\sqrt{2})(|0\rangle + |1\rangle)$. After evolution for time t, the N-V-center spin state evolves to

$$|\psi(t)\rangle = \exp\left[(-it\Omega_1/2)\sigma_x\right]\exp\left[(-it\Omega_2/2)\sigma_z\right]|\psi(0)\rangle\,. \tag{A6}$$

The fluorescence measurement after another $(\pi/2)_y$ pulse gives the state population:

$$P_{|0\rangle} = |\langle\psi(0)|\psi(t)\rangle|^2 = \frac{1}{2}\left[1 + \cos(\Omega_1 t)\cos(\Omega_2 t)\right]. \tag{A7}$$

Two frequency components Ω_1 and Ω_2, in addition to the effect of unpolarized nitrogen nuclear spin, lead to the beating pattern in the oscillating signal, which explains our experimental observation and is also verified by numerical simulation. The extended coherence time can be inferred from the decay of the envelope.

APPENDIX B: CHARACTERISTICS OF NANODIAMONDS

The nanodiamonds are spin-coated on a mica plate and scanned after drying. We choose different areas to perform an AFM scan and count the distribution of nanodiamond size. Considering the broadening effect of the AFM, we measure the height of nanodiamonds to estimate their sizes. The nanodiamond size distribution is shown in Fig. 1(b). The average nanodiamond size is about 43 nm, with the diameters predominantly within 25–60 nm (43 ± 18 nm), and the nanodiamond concentration is about 50 per 100 μm^2.

To characterize the properties of spin noise, we perform a Ramsey measurement by applying magnetic fields of different strength along the N-V axis. The dependence of T_2^* on the applied magnetic field is shown in Fig. 5. It can be seen that T_2^* increases with a larger magnetic field, which suggests that electric noise may be a dominant source of spin dephasing in the present sample [41]. We also perform spin-echo measurement of N-V centers in several nanodiamonds. Owing to the different environments for different nanodiamond N-V centers, they exhibit different coherence times. The experimental data are normalized through Rabi oscillation, and are then fitted with the

TABLE I. Spin-echo measurement for nanodiamond N-V centers. The normalized experimental data are fitted with the function $P_{|0\rangle}(t) = (1/2)\left(1 + e^{-(t/T_{\text{SE}})^\alpha}\right)$. The estimated values of T_{SE} and α for eight nanodimonad N-V centers are listed.

	1	2	3	4	5	6	7	8
T_2 (μs)	4.840 ± 0.009	4.300 ± 0.069	2.142 ± 0.018	1.30 ± 0.24	4.292 ± 0.133	8.710 ± 0.203	2.990 ± 0.083	2.711 ± 0.078
α	1.082 ± 0.045	1.542 ± 0.056	1.448 ± 0.026	1.447 ± 0.295	1.47 ± 0.10	1.392 ± 0.068	1.576 ± 0.101	1.740 ± 0.113

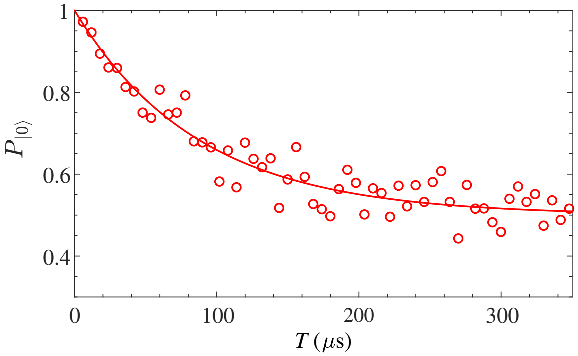

FIG. 6. Relaxation time of nanodiamond N-V. The normalized experimental data are fitted with the function $P_{|0\rangle}(t) = (1/2)\left(1 + e^{-(t/T_1)}\right)$. The applied magnetic field $B_{\parallel} = 508$ G. The relaxation time T_1 is estimated to be 87.35 ± 7.50 μs.

function $P_{|0\rangle}(t) = (1/2)\{1 + \exp[-(t/T_{\mathrm{SE}})^{\alpha}]\}$. The results show that $\alpha \in [1.08, 1.74]$ and that T_{SE} for the average spin-echo coherence time is around 3 μs; see Table I. In Fig. 6, we plot the experimental data for the relaxation-time measurement of the N-V center shown in Fig. 2. The normalized experimental data are fitted with the function $P_{|0\rangle}(t) = (1/2)\{1 + \exp[-(t/T_1)]\}$, which gives an estimation of $T_1 = 87.35 \pm 7.50$ μs.

In the main text, we present experiments in which we apply XY8-N pulse sequences to extend the coherence time of N-V centers using a train of $(8 \times N)$ π pulses. The extended coherence time T_2 under pulsed dynamical decoupling increases as the number of XY8 cycles increases, and reaches a saturated value. For Fig. 4(a), we apply π pulses with different peak Rabi frequencies and measure the achievable saturated coherence time. The average microwave power can be quantified by the average effective Rabi frequency, which is defined as follows

$$\bar{\Omega} = \left(\frac{1}{T}\int_0^T \Omega^2(t)dt\right)^{1/2}. \tag{B1}$$

In Table II, we list the peak Rabi frequency, the average effective Rabi frequency, and the number of XY8 cycles of the pulse sequences that achieve the longest coherence time as shown in Fig. 4(a).

APPENDIX C: CELL CULTURE AND SAMPLE PREPARATION

NIH/3T3 cells are cultured in Dulbecco's modified Eagle's medium (DMEM) supplemented with fetal bovine serum and penicillin-streptomycin. Nanodiamonds are diluted in DMEM. Then cells are seeded on coverslips and incubated with the DMEM-nanodiamond suspension (37 °C, 5% CO_2) for 20 h, which allows cells to adhere to the surface of the cover glass. After treatment, the medium is removed and the cover glass is washed 3 times with PBS. The cultured NIH/3T3 cells are immersed in PBS throughout the measurement, and the temperature is kept at around 22 °C. The confocal imaging is performed through the cover glass, with an oil-immersion lens. The N-V center measured in this work is located about 2.5 μm above the cover glass. Quantum measurements are performed on the N-V centers by our applying a microwave signal along a copper wire (with a diameter of approximately 20 μm) that is about 30 μm from the N-V center.

APPENDIX D: CELL-MEMBRANE STAINING AND IDENTIFICATION OF NANODIAMONDS IN CELLS

To identify those nanodiamonds that were taken up cells, we first use 1,1′-Dioctadecyl-3,3,3′,3′-tetramethylindocarbocyanine perchlorate [$\mathrm{DiIC}_{18}(3)$], which is a lipophilic fluorescent dye, to label the cytomembrane. After cellular uptake, the cell culture medium is removed, and the cells are then incubated with 200 μl of $\mathrm{DiIC}_{18}(3)$ (0.0486 μM) solution for about 1 h (37 °C, 5% CO_2). The sample is washed 5 times with PBS before it is imaged with a homebuilt confocal setup. Stained-cell images with a clear profile are shown in Figs. 7(a) and 7(c), which demonstrate clearly the cytomembrane labeled by $\mathrm{DiIC}_{18}(3)$ and the cell nucleus. Figure 7(b) shows an enlarged area where we identify three nanodiamonds in the cell, which is further confirmed by our X-Z confocal scan; see Figs. 7(d)–7(f).

APPENDIX E: INFLUENCE OF MICROWAVE RADIATION ON LIVING CELLS

The main influence of microwave radiation on living cells arises from the heating effect. We perform measurements to clarify the following two issues: (i) the dependence of the heating effect on the microwave power; (ii) whether the difference in the microwave power required

TABLE II. Detailed information on the XY8 pulse sequences that achieve the coherence time of N-V centers in nanodiamond as shown in Fig. 4(a).

	1	2	3	4	5
Peak Rabi frequency (MHz)	1.98	5.10	7.14	8.50	16.20
Average effective Rabi frequency (MHz)	1.94	4.13	4.89	5.19	8.25
XY8 cycles	6	12	12	12	14

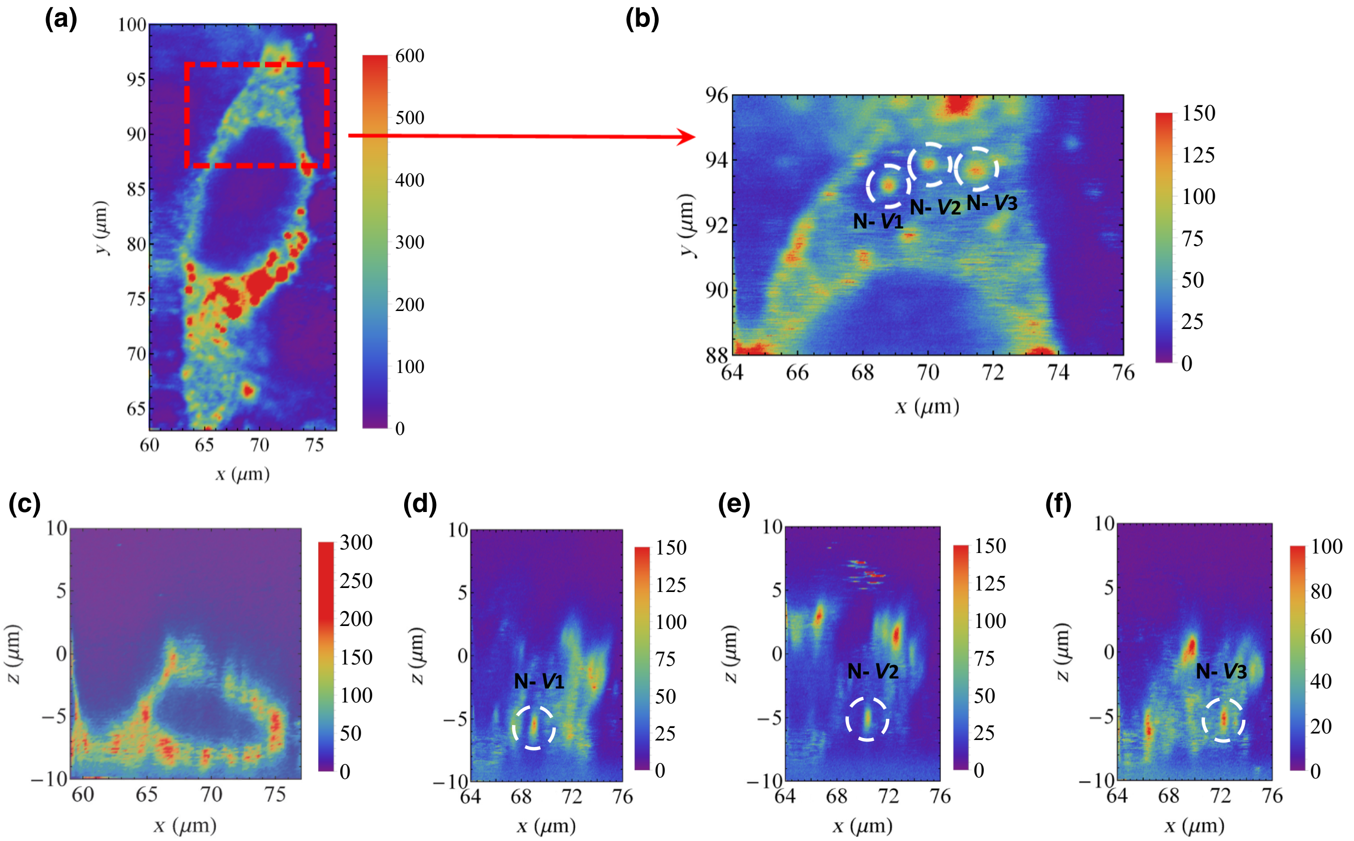

FIG. 7. (a) Confocal scan of a living cell with cytomembrane labeled with a lipophilic fluorescent dye. The enlarged area in the dashed rectangle is shown in (b). Three nanodiamonds are identified in the cell, which is confirmed by *X*-*Z* scan as shown in (c)–(f). The photon count is in the unit of 1000 counts/s.

to achieve the same coherence times under the pulsed and CCDD schemes matters (i.e., whether it may lead to a non-negligible difference in the heating of the sample). The role of microwave power in the manipulation of N-*V* centers is manifested by the observed Rabi frequency. In Fig. 8, we calibrate the dependence of the Rabi frequency on the amplitude of the AWG output by measuring Rabi frequencies for several N-*V* centers in nanodiamond when applying magnetic fields of different strengths. The measurements show that the Rabi frequencies are proportional to the amplitude of the AWG output, which is quantified by the peak-to-peak voltage. The results also provide information on the microwave power required to achieve a certain Rabi frequency. For example, the Rabi frequency is increased by 3–6 MHz with an increase of the AWG output amplitude of 100 mV for typical nanodiamonds that locate within a distance of 5–15 μm to the microwave wire. For the measurements in Fig. 4, a Rabi frequency of 9.6 MHz (4.6 MHz) is achieved with an AWG output of 400 mV (200 mV) and 30% (25%) amplification percentage. As $\Omega_2 \ll \Omega_1$, one can easily verify that the microwave radiation power is determined by the amplitude Ω_1.

It has been shown that the main damage from microwave radiation applied to cells is caused by the heating effect. The viability of cells may be influenced substantially as the temperature increases by 10 °C; see, for example, Refs. [46,47]. In our experiments, we apply microwaves with the pulsed and CCDD schemes and

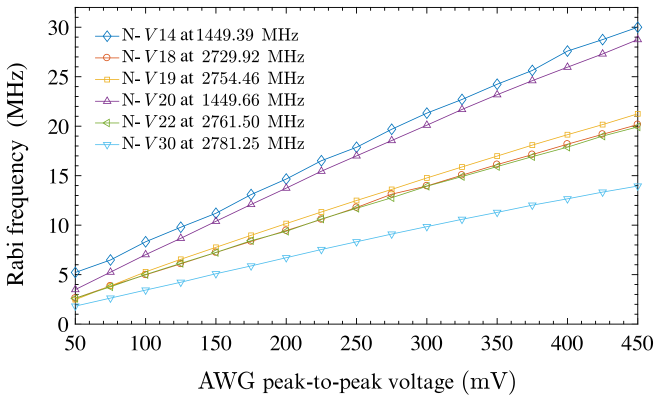

FIG. 8. Dependence of the Rabi frequency on the peak-to-peak voltage of the AWG output for several N-*V* centers in nanodiamond. Rabi measurements are performed at frequencies as shown when different magnetic fields are applied along the N-*V* axis. The amplification percentage of the amplifier is fixed at 45%.

monitor the temperature of the sample under similar conditions in the experiments as presented in the main text. We glue a coverslip (2.4×2.4 cm^2), to which cells adhere and grow, on a printed circuit board in contact with a copper wire that delivers microwaves. A thermistor (Thorlabs TH10K) attached to the coverslip allows us measure the temperature of the sample when applying microwave sequences. We add 1 ml PBS, which is used to maintain gentle conditions for living cells.

We denote the peak-to-peak voltage of the AWG output as A (millivolts), which quantifies the peak power of microwave radiation. We first apply the CCDD scheme with the following parameters: the duration of continuous microwave driving T_{on} is 30 μs (which is similar to the extended coherence time as observed in our experiment; the combination of the laser pulse and idle time T_{off} is set as 3.8 μs (which is similar to the corresponding time in our experiments). As there is time during which microwave radiation is switched off, we define the average amplitude of microwave radiation as follows:

$$\langle A\rangle = A\sqrt{\frac{T_{\text{on}}}{T_{\text{on}}+T_{\text{off}}}}. \tag{E1}$$

We monitor the temperature of the sample every 60 s and record the stable temperature, which is usually reached in approximately 15 min. The results are shown in Fig. 9 as blue circles. For comparison, we also apply the XY8-12 scheme (i.e., the total number of pulses N is 96) with the following parameters: the π-pulse duration τ_π is 50 ns; the time between pulses (i.e., no microwaves) τ_f is 100 or (4) ns; the combination of laser pulse and idle time T_{off} is set as 3.8 μs. In this case, the average amplitude of microwave radiation is given by

$$\langle A\rangle = A\sqrt{\frac{N\tau_\pi}{N\tau_\pi+N\tau_f+T_{\text{off}}}}. \tag{E2}$$

The results are shown in Fig. 9 (red squares for $\tau_f = 100$ ns and red diamonds for $\tau_f = 4$ ns). Although we choose certain specific parameters for the pulses (which are close to those parameters used in our experiments), we find that the heating effect is determined mainly by the *average* microwave power [as quantified by the average amplitude of the AWG output defined in Eqs. (E1) and (E2)] for both the pulsed scheme and the CCDD scheme, while is weakly dependent on the details of the microwave pulses. The sample temperature increases by approximately 12 °C when the average amplitude of the AWG output increases by 100 mV (which corresponds to an increase in the Rabi frequency of approximately 3–5 MHz). The exact difference in the heating effect may also depend on other factors, such as the distance from the microwave wire to the N-V center; nevertheless, our measurement strongly suggests that the more-stringent requirement with regard to the microwave power in pulsed schemes will result in a severer heating effect on biological tissues. For example, we compare the data in Fig. 4. The average microwave power for CCDD to achieve a coherence time of approximately 15 μs is less than 1 MHz, while 4–5 MHz is required for the pulsed scheme. Therefore, according to the observed characteristics of the heating effect due to microwave radiation, the temperature increase due to the pulsed sequences will be about 10 °C more than that due to the CCDD scheme, which can be expected to have a significant effect on biological tissues [46,47].

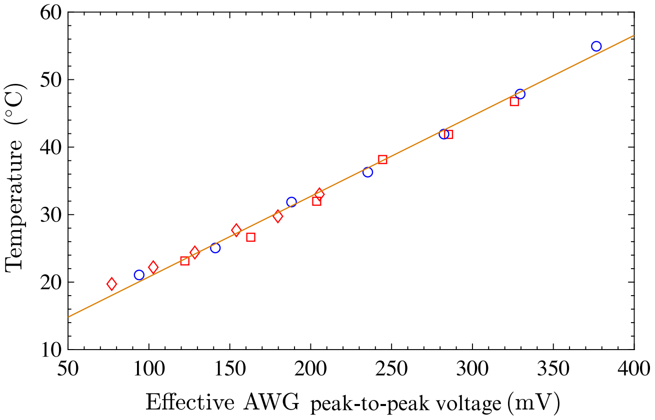

FIG. 9. Increase of sample temperature as a function of the average amplitude of the AWG output. The amplification percentage of the amplifier is fixed at 45%. The results for the CCDD scheme are shown in blue circles, and those for the pulsed scheme are shown in red squares and diamonds.

APPENDIX F: SENSITIVITY COMPARISON UNDER THE CONSTRAINT OF MICROWAVE POWER

We consider a typical scenario of quantum sensing; namely, the detection of a weak oscillating magnetic field $b(t) = b\cos\omega_s t$ with frequency ω_s and amplitude b. The underlying principle is similar to the detection of electron (nuclear) spin, where the characteristic frequency is the Larmor frequency of the target spins. One possible interesting example is the detection of radicals inside cells. In N-V-spin-sensor-based magnetic spectroscopy, the Larmor frequency of the target spins will usually exceed approximately 10 MHz (e.g., for electron spin or nuclear spin in high-field magnetic resonance spectroscopy). Depending on the relative orientation of the magnetic field with respect to the N-V axis (denoted as the $\hat{z}$ axis that connects the nitrogen atom and the vacancy site) and the field frequency ω_s, the N-V-center spin sensor may be sensitive to the field components along either the $\hat{z}$ direction or the $\hat{x}$ direction. To investigate the achievable measurement sensitivity under the constraint of microwave power, we denote the available (maximum) Rabi frequency as $\Omega_{\max}$.

We first consider quantum sensing in combination with the present CCDD scheme. In the first case of $\omega_s \leq \Omega_{\max}$, we can choose to measure the field along the $\hat{z}$ direction by tuning the orientation of the N-V axis in parallel with the polarization of the magnetic field. In the interaction picture, when we set $\Omega_1 = \omega_s$, the effective Hamiltonian becomes

$$H_2 = (\Omega_2/2)\sigma_z + (\gamma b/2)\sigma_z, \tag{F1}$$

where γ is the electronic gyromagnetic ratio [37]. The field parameter b can be determined via a Ramsey experiment, and the measurement sensitivity with interrogation time $t = T_c$ is estimated to be given by

$$\eta_c = \frac{\sqrt{\Delta^2 p}}{C(\partial p/\partial b)\sqrt{1/T_c}} \simeq 1/\gamma C\sqrt{T_c}, \tag{F2}$$

where T_c is the extended coherence time, $p = (1/2)(1 + \cos\gamma b T_c)$ is the signal in the Ramsey experiment, and C represents the detection efficiency [4]. As $\omega_s \leq \Omega_{\max}$, it is always feasible to choose Rabi frequency $\Omega_1 = \omega_s$. In the second case of $\omega_s > \Omega_{\max}$, we choose to measure the field along the $\hat{x}$ direction by tuning the orientation of the N-V axis perpendicular to the polarization of the magnetic field. In the interaction picture, when we set $\Omega_1 = \omega_0 - \omega_s$, the effective Hamiltonian becomes [37]

$$H_3 = -(\gamma b/4)\sigma_z. \tag{F3}$$

The measurement sensitivity via a Ramsey experiment with interrogation time $t = T_c$ is estimated to be given by

$$\eta_c = \frac{\sqrt{\Delta^2 p}}{C(\partial p/\partial b)\sqrt{1/T_c}} \simeq 2/\gamma C\sqrt{T_c}, \tag{F4}$$

where the signal in the Ramsey experiment is given by $p = (1/2)\,[1 + \cos(\gamma b T_c/2)]$.

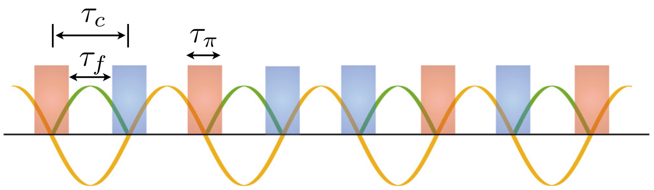

FIG. 10. Pulsed scheme with noninstantaneous π pulses. The π-pulse duration is denoted as $\tau_\pi = \pi/\Omega$, where Ω is the Rabi frequency of the pulses. The interpulse free evolution time is τ_f. The time interval $\tau_c = \tau_\pi + \tau_f$ between pulses should match the oscillating field frequency; namely, $\tau_c = k(\pi/\omega_s)$, where $k = 1, 3, 5, \ldots$. The role of π pulses is to change the sign of the magnetic field acting on the N-V-center spin so that its effect can be accumulated constructively.

The pulsed scheme detects an oscillating field by engineering the time interval τ_c between pulses (see Fig. 10) to match the field frequency; namely, $\tau_c = k(\pi/\omega_s)$ [14]. For ideal instantaneous π pulses (i.e., requiring infinite microwave power), $\tau_c = \tau_f$, where τ_f is the free evolution between pulses. In our experiment, we first apply a $(\pi/2)_y$ pulse to prepare the N-V-center spin in a superposition state $|\psi(0)\rangle = (1/\sqrt{2})(|0\rangle + |1\rangle)$. After interrogation for time t, the N-V-center spin state evolves to the following state as

$$|\psi(t)\rangle = \exp\left[-i\gamma b(2/\pi)t\sigma_z\right]|\psi(0)\rangle\,. \tag{F5}$$

The factor $2/\pi$ comes from the average of the modulated oscillating field. The state population measurement after another $(\pi/2)_y$ pulse leads to the signal in the Ramsey experiment as follows:

$$p = |\langle\psi(0)|\psi(t)\rangle|^2 = \frac{1}{2} + \frac{1}{2}\cos\left[\gamma b(4/\pi)t\right]. \tag{F6}$$

The estimated measurement sensitivity with interrogation time T_2 is

$$\eta_p = \frac{\sqrt{\Delta^2 p}}{C(\partial p/\partial b)\sqrt{1/T_2}} \simeq k\pi/4\gamma C\sqrt{T_2}. \tag{F7}$$

Given a field with frequency ω_s, the required power is Ω^2 for the CCDD scheme with $\Omega = \omega_s$. For the pulsed scheme, the pulse repetition rate should be π/ω_s; namely, the time interval between two pulses $\tau_c = k(\pi/\omega_s)$. The pulse duration τ_π should be much smaller than τ_c (see Fig. 10); namely, the ratio $a = \tau_\pi/\tau_c \ll 1$. Thus, one can estimate that the power required for the pulsed scheme is Ω^2/a. It can be seen that the power required for the CCDD scheme is less than that required for the pulsed scheme by a factor of $a = \tau_\pi/\tau_c \ll 1$.

For noninstantaneous π pulses realized by finite microwave power, $\tau_p = \tau_\pi + \tau_f$, where $\tau_\pi = \pi/\Omega$ is the pulse duration and τ_f is the free evolution between pulses; see Fig. 10. As we are considering the pulsed scheme, we require $\tau_f > 0$, otherwise the pulsed scheme would become continuous. However, the limited pulse Rabi frequency Ω (in comparison with the field frequency ω_s) leads to a constraint on the resonant condition $k \geq \omega_s/\Omega$ and will decrease the signal contrast. In Fig. 11, we show the signal contrast for the measurement of an oscillating magnetic field with different frequencies using pulses of the same duration (namely, the same available Rabi frequency). It can be seen that the signal contrast decreases with increasing field frequency; see Fig. 11(a). This is also confirmed by the less-steep signal slope $(\partial p/\partial b)$ for an oscillating field with a higher frequency ω_s; see Fig. 11(b). In Fig. 4, we compare the estimated measurement sensitivities for the CCDD and pulsed schemes according

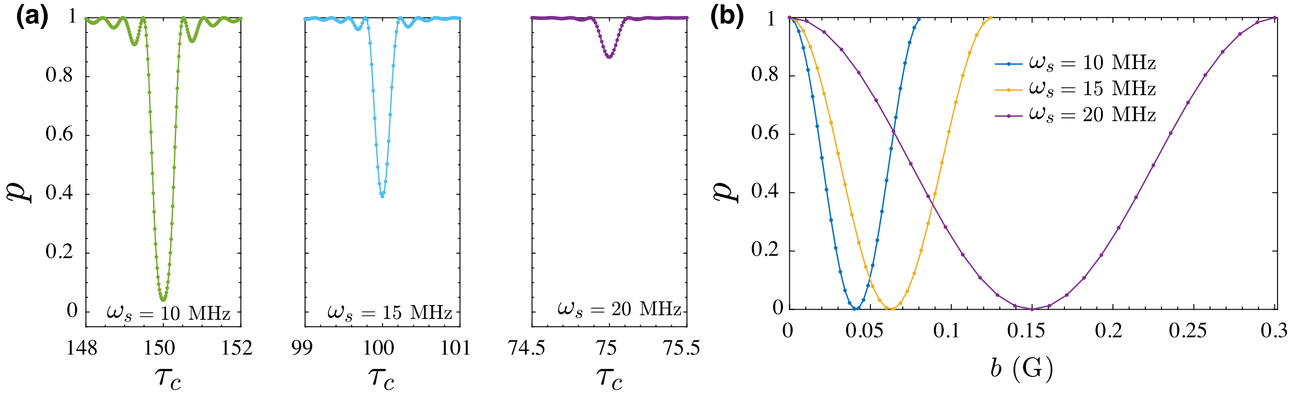

FIG. 11. Quantum sensing using the pulsed scheme with noninstantaneous π pulses. (a) Signal as a function of the time interval close to the resonant condition $\tau_c = 3(\pi/\omega_s)$ for an oscillating magnetic field with different frequencies $\omega_s = 10, 15$, and 20 MHz. The field strength $\gamma b = 2\pi \times 100$ kHz. (b) The signal p as a function of the oscillating field strength b. In (a),(b), the interrogation time T_2 is set as 15.22 μs. The pulse Rabi frequency $\Omega = 8.5$ MHz.

to the coherence time achieved. The enhanced sensitivity of the present CCDD scheme arises from both the prolonged coherence time and the limit of microwave-power constraint in the pulsed scheme.

[1] M. W. Doherty, N. B. Manson, P. Delaney, F. Jelezko, J. Wrachtrup, and L. C. L. Hollenberg, The nitrogen-vacancy colour centre in diamond, Phys. Rep. **528**, 1 (2013).

[2] J. R. Maze, P. L. Stanwix, J. S. Hodges, S. Hong, J. M. Taylor, P. Cappellaro, L. Jiang, M. V. G. Dutt, E. Togan, A. S. Zibrov, A. Yacoby, R. L. Walsworth, and M. D. Lukin, Nanoscale magnetic sensing with an individual electronic spin in diamond, Nature (London) **455**, 644 (2008).

[3] G. Balasubramanian, I. Y. Chan, R. Kolesov, M. Al-Hmoud, J. Tisler, C. Shin, C. Kim, A. Wojcik, P. R. Hemmer, A. Krueger, T. Hanke, A. Leitenstorfer, R. Bratschitsch, F. Jelezko, and J. Wrachtrup, Nanoscale imaging magnetometry with diamond spins under ambient conditions, Nature (London) **455**, 648 (2008).

[4] J. M. Taylor, P. Cappellaro, L. Childress, L. Jiang, D. Budker, P. R. Hemmer, A. Yacoby, R. Walsworth, and M. D. Lukin, High-sensitivity diamond magnetometer with nanoscale resolution, Nat. Phys. **4**, 810 (2008).

[5] F. Dolde, H. Fedder, M. W. Doherty, T. Nobauer, F. Rempp, G. Balasubramanian, T. Wolf, F. Reinhard, L. C. L. Hollenberg, F. Jelezko, and J. Wrachtrup, Electric-field sensing using single diamond spins, Nat. Phys. **7**, 459 (2011).

[6] F. Dolde, M. W. Doherty, J. Michl, I. Jakobi, B. Naydenov, S. Pezzagna, J. Meijer, P. Neumann, F. Jelezko, N. B. Manson, and J. Wrachtrup, Nanoscale Detection of a Single Fundamental Charge in Ambient Conditions Using the NV$^-$ Center in Diamond, Phys. Rev. Lett. **112**, 097603 (2014).

[7] V. M. Acosta, E. Bauch, M. P. Ledbetter, A. Waxman, L.-S. Bouchard, and D. Budker, Temperature Dependence of the Nitrogen-Vacancy Magnetic Resonance in Diamond, Phys. Rev. Lett. **104**, 070801 (2010).

[8] G. Kucsko, P. C. Maurer, N. Y. Yao, M. Kubo, H. J. Noh, P. K. Lo, H. Park, and M. D. Lukin, Nanometre-scale thermometry in a living cell, Nature **500**, 54 (2013).

[9] D. M. Toyli, C. F. de las Casas, D. J. Christle, V. V. Dobrovitski, and D. D. Awschalom, Fluorescence thermometry enhanced by the quantum coherence of single spins in diamond, Proc. Natl. Acad. Sci. U.S.A. **110**, 8417 (2013).

[10] P. Neumann, I. Jakobi, F. Dolde, C. Burk, R. Reuter, G. Waldherr, J. Honert, T. Wolf, A. Brunner, J. H. Shim, D. Suter, H. Sumiya, J. Isoya, and J. Wrachtrup, High-precision nanoscale temperature sensing using single defects in diamond, Nano Lett. **13**, 2738 (2013).

[11] M. W. Doherty, V. V. Struzhkin, D. A. Simpson, L. P. McGuinness, Y.-F. Meng, A. Stacey, T. J. Karle, R. J. Hemley, N. B. Manson, L. C. L. Hollenberg, and S. Prawer, Electronic Properties and Metrology Applications of the Diamond NV$^-$ Center under Pressure, Phys. Rev. Lett. **112**, 047601 (2014).

[12] J.-M. Cai, F. Jelezko, and M. B. Plenio, Hybrid sensors based on colour centres in diamond and piezoactive layers, Nat. Commun. **5**, 4065 (2014).

[13] R. Schirhagl, K. Chang, M. Loretz, and C. L. Degen, Nitrogen-vacancy centers in diamond: Nanoscale sensors for physics and biology, Annu. Rev. Phys. Chem. **65**, 83 (2014).

[14] C. L. Degen, F. Reinhard, and P. Cappellaro, Quantum sensing, Rev. Mod. Phys. **89**, 035002 (2017).

[15] M. Hirose, C. D. Aiello, and P. Cappellaro, Continuous dynamical decoupling magnetometry, Phys. Rev. A **86**, 062320 (2012).

[16] K. Fang, V. M. Acosta, C. Santori, Z. Huang, K. M. Itoh, H. Watanabe, S. Shikata, and R. G. Beausoleil, High-Sensitivity Magnetometry Based on Quantum Beats in Diamond Nitrogen-Vacancy Centers, Phys. Rev. Lett. **110**, 130802 (2013).

[17] A. Cooper, E. Magesan, H. Yum, and P. Cappellaro, Time-resolved magnetic sensing with electronic spins in diamond, Nat. Commun. **5**, 3141 (2014).

[18] L. T. Hall, P. Kehayias, D. A. Simpson, A. Jarmola, A. Stacey, D. Budker, and L. C. L. Hollenberg, Detection of nanoscale electron spin resonance spectra demonstrated using nitrogen-vacancy centre probes in diamond, Nat. Commun. **7**, 10211 (2016).

[19] T. Joas, A. M. Waeber, G. Braunbeck, and F. Reinhard, Quantum sensing of weak radio-frequency signals by pulsed mollow absorption spectroscopy, Nat. Commun. **8**, 964 (2017).

[20] A. Stark, N. Aharon, T. Unden, D. Louzon, A. Huck, A. Retzker, U. L. Andersen, and F. Jelezko, Narrow-bandwidth sensing of high-frequency fields with continuous dynamical decoupling, Nat. Commun. **8**, 1105 (2017).

[21] S. Schmitt, T. Gefen, F. M. Stürner, T. Unden, G. Wolff, C. Müller, J. Scheuer, B. Naydenov, M. Markham, S. Pezzagna, J. Meijer, I. Schwarz, M. Plenio, A. Retzker, L. P. McGuinness, and F. Jelezko, Submillihertz magnetic spectroscopy performed with a nanoscale quantum sensor, Science **356**, 832 (2017).

[22] J. M. Boss, K. S. Cujia, J. Zopes, and C. L. Degen, Quantum sensing with arbitrary frequency resolution, Science **356**, 837 (2017).

[23] Haibin Liu, Martin B. Plenio, and Jianming Cai, Scheme for Detection of Single-Molecule Radical Pair Reaction Using Spin in Diamond, Phys. Rev. Lett. **118**, 200402 (2017).

[24] S. Hsieh, P. Bhattacharyya, C. Zu, T. Mittiga, T. J. Smart, F. Machado, B. Kobrin, T. O. Höhn, N. Z. Rui, M. Kamrani, S. Chatterjee, S. Choi, M. Zaletel, V. V. Struzhkin, J. E. Moore, V. I. Levitas, R. Jeanloz, and N. Y. Yao, Imaging stress and magnetism at high pressures using a nanoscale quantum sensor, Science **366**, 1349 (2019).

[25] King Yau Yip, Kin On Ho, King Yiu Yu, Yang Chen, Wei Zhang, S. Kasahara, Y. Mizukami, T. Shibauchi, Y. Matsuda, Swee K. Goh, and Sen Yang, Measuring magnetic field texture in correlated electron systems under extreme conditions, Science **366**, 1355 (2019).

[26] Margarita Lesik, Thomas Plisson, L. Toraille, J. Renaud, F. Occelli, M. Schmidt, O. Salord, A. Delobbe, T. Debuisschert, L. Rondin, P. Loubeyre, and J.-F. Roch, Magnetic measurements on micrometer-sized samples under high pressure using designed NV centers, Science **366**, 1359 (2019).

[27] G. Balasubramanian, P. Neumann, D. Twitchen, M. Markham, R. Kolesov, N. Mizuochi, J. Isoya, J. Achard, J. Beck, J. Tissler, V. Jacques, P. R. Hemmer, F. Jelezko, and J. Wrachtrup, Ultralong spin coherence time in isotopically engineered diamond, Nat. Mater. **8**, 382 (2009).

[28] G. de Lange, Z. H. Wang, D. Ristè, V. V. Dobrovitski, and R. Hanson, Universal dynamical decoupling of a single solid-state spin from a spin bath, Science **330**, 60 (2010).

[29] B. Naydenov, F. Dolde, L. T. Hall, C. Shin, H. Fedder, L. C. L. Hollenberg, F. Jelezko, and J. Wrachtrup, Dynamical decoupling of a single-electron spin at room temperature, Phys. Rev. B **83**, 081201 (2011).

[30] H. S. Knowles, D. M. Kara, and M. Ataüre, Observing bulk diamond spin coherence in high-purity nanodiamonds, Nat. Mater. **13**, 21 (2014).

[31] L. P. McGuinness, Y. Yan, A. Stacey, D. A. Simpson, L. T. Hall, D. Maclaurin, S. Prawer, P. Mulvaney, J. Wrachtrup, F. Caruso, R. E. Scholten, and L. C. Hollenberg, Quantum measurement and orientation tracking of fluorescent nanodiamonds inside living cells, Nat. Nanotechnol. **6**, 358 (2011).

[32] D. Le Sage, K. Arai, D. R. Glenn, S. J. DeVience, L. M. Pham, L. Rahn-Lee, M. D. Lukin, A. Yacoby, A. Komeili, and R. L. Walsworth, Optical magnetic imaging of living cells, Nature **496**, 486 (2013).

[33] G. Balasubramanian, A. Lazariev, S. R. Arumugam, and De-wen Duan, Nitrogen-vacancy color center in diamond-emerging nanoscale applications in bioimaging and biosensing, Curr. Opin. Chem. Biol. **20**, 69 (2014).

[34] Y. Wu, F. Jelezko, M. B. Plenio, and T. Weil, Diamond quantum devices in biology, Angewandte Chemie - International Edition **55**, 6586 (2016).

[35] G. Gordon, G. Kurizki, and D. A. Lidar, Optimal Dynamical Decoherence Control of a Qubit, Phys. Rev. Lett. **101**, 010403 (2008).

[36] J.-M. Cai, B. Naydenov, R. Pfeiffer, L. McGuinness, K. Jahnke, F. Jelezko, M. B. Plenio, and A. Retzker, Robust dynamical decoupling with concatenated continuous driving, New J. Phys. **14**, 113023 (2012).

[37] I. Cohen, N. Aharon, and A. Retzker, Continuous dynamical decoupling utilizing time-dependent detuning, Fortschr. Phys. **64**, 1521 (2016).

[38] D. Farfurnik, N. Aharon, I. Cohen, Y. Hovav, A. Retzker, and N. Bar-Gill, Experimental realization of time-dependent phase-modulated continuous dynamical decoupling, Phys. Rev. A **96**, 013850 (2017).

[39] Zijun Shu, Yu Liu, Qingyun Cao, Pengcheng Yang, Shaoliang Zhang, Martin B. Plenio, Fedor Jelezko, and Jianming Cai, Observation of Floquet Raman Transition in a Driven Solid-State Spin System, Phys. Rev. Lett. **121**, 210501 (2018).

[40] M. Yu, P.-C. Yang, M.-S. Gong, Q.-Y. Cao, Q.-Y. Lu, H.-B. Liu, M. B. Plenio, F. Jelezko, T. Ozawa, N. Goldman, S.-L. Zhang, and J.-M. Cai, Experimental measurement of the quantum geometric tensor using coupled qubits in diamond, Natl. Sci. Rev. nwz193 (2019).

[41] P. Jamonneau, M. Lesik, J. P. Tetienne, I. Alvizu, L. Mayer, A. Dréau, S. Kosen, J.-F. Roch, S. Pezzagna, J. Meijer, T. Teraji, Y. Kubo, P. Bertet, J. R. Maze, and V. Jacques, Competition between electric field and magnetic field noise in the decoherence of a single spin in diamond, Phys. Rev. B **93**, 024305 (2016).

[42] J. Medford, Ł. Cywiński, C. Barthel, C. M. Marcus, M. P. Hanson, and A. C. Gossard, Scaling of Dynamical Decoupling for Spin Qubits, Phys. Rev. Lett. **108**, 086802 (2012).

[43] M. A. Ali Ahmed, G. A. Álvarez, and D. Suter, Robustness of dynamical decoupling sequences, Phys. Rev. A **87**, 042309 (2013).

[44] N. Aharon, I. Cohen, F. Jelezko, and A. Retzker, Fully robust qubit in atomic and molecular three-level systems, New J. Phys. **18**, 123012 (2016).

[45] N. Bar-Gill, L. M. Pham, A. Jarmola, D. Budker, and R. L. Walsworth, Solid-state electronic spin coherence time approaching one second, Nat. Commun. **4**, 1743 (2013).

[46] Im-Sun Woo, In-Koo Rhee, and Heui-Dong Park, Differential damage in bacterial cells by microwave radiation on

the basis of cell wall structure, Appl. Environ. Microbiol. **66**, 2243 (2000).

[47] Y. Shamis, R. Croft, A. Taube, R. J. Crawford, and E. P. Ivanova, Review of the specific effects of microwave radiation on bacterial cells, Appl. Microbiol. Biotechnol. **96**, 319 (2012).

[48] M. Loretz, J. M. Boss, T. Rosskopf, H. J. Mamin, D. Rugar, and C. L. Degen, Spurious Harmonic Response of Multipulse Quantum Sensing Sequences, Phys. Rev. X **5**, 021009 (2015).

[49] J. F. Haase, Z.-Y. Wang, J. Casanova, and M. B. Plenio, Pulse-phase control for spectral disambiguation in quantum sensing protocols, Phys. Rev. A **94**, 032322 (2016).

[50] Z.-J. Shu, Z.-D. Zhang, Q.-Y. Cao, P.-C. Yang, M. B. Plenio, C. Müller, J. Lang, N. Tomek, B. Naydenov, L. P. McGuinness, F. Jelezko, and J.-M. Cai, Unambiguous nuclear spin detection using an engineered quantum sensing sequence, Phys. Rev. A **96**, 051402 (2017).